ABSTRACT

IGNITION OF METAL POWDER BY ELECTROSTATIC DISCHARGE STIMULATION

by
Ervin Beloni

Energetic formulations with metal fuel additives are extensively used in propellants, explosives, pyrotechnics, and incendiaries. Currently, replacement of regular metal powders with nanocomposite metal-based materials is being considered. Such nanocomposite reactive materials are capable of very high reaction rates while maintaining the high combustion enthalpies characteristic of metals. However, such novel reactive nano-materials are often highly sensitive to impact, friction, and electrostatic discharge, making them difficult to handle. In particular, their high electrostatic discharge sensitivity (ESD) was reported. While ESD testing is very common and standardized, the mechanisms of powder ignition by electric spark remain unclear. This project is aimed to establish the relationship between thermal ignition mechanism for metal powders and related nanocomposites and their ESD sensitivity. The project includes both experimental and modeling components. An explicit numerical model of the heat transfer within a powder bed subject to a pulsed electric discharge will be developed. The model will initially describe the behavior of metal powders for which the thermal ignition kinetics is well established and quantified, such as spherical magnesium. It will be further expanded for novel nanocomposite materials for which the kinetics of exothermic processes leading to ignition will be determined in separate experiments. The predictions will be validated experimentally using a standard ESD testing apparatus with additional optical sensors and electronic diagnostics.

IGNITION OF METAL POWDER
BY ELECTROSTATIC DISCHARGE STIMULATION

by
Ervin Beloni

A Thesis
Submitted to the Faculty of
New Jersey Institute of Technology
in Partial Fulfillment of the Requirements for the Degree of
Master of Science in Mechanical Engineering

Department of Mechanical Engineering

January 2008

APPROVAL PAGE

IGNITION OF METAL POWDER BY ELECTROSTATIC DISCHARGE STIMULATION

Ervin Beloni

Dr. Edward L. Dreizin, Thesis Advisor — Date
Professor of Chemical Engineering, NJIT

Dr. Boris Khusid, Committee Member — Date
Professor of Chemical Engineering, NJIT

Dr. Mirko Schoenitz, Committee Member — Date
Assistant Research Professor of Chemical Engineering, NJIT

BIOGRAPHICAL SKETCH

Author: Ervin Beloni

Degree: Master of Science

Date: January 2008

Undergraduate and Graduate Education:

- Master of Science in Mechanical Engineering,
  New Jersey Institute of Technology, Newark, NJ, 2008

- Bachelor of Science in Mechanical Engineering,
  New Jersey Institute of Technology, Newark, NJ, 2006

Major: Mechanical Engineering

Presentations:

Ervin Beloni, Mikhaylo A. Trunov, Eric Whitman and Edward L. Dreizin,
"Ignition of metal powders by electric spark,"
2007 AICHE Annual Meeting, Salt Lake City, UT, November 2007.

Ervin Beloni and Edward L. Dreizin,
"Development of Insensitive High Energy Density Nanomaterials,"
AIAA Region I-NE Student Conference, Cambridge, MA, April 2007.

Ervin Beloni, Vern K. Hoffmann, and Edward L. Dreizin,
"Combustion of Decane-based Slurries with Metallic Fuel Additives,"
45th AIAA Aerospace Sciences Meeting, Reno, NV, January 2007.

Ervin Beloni, Vern K. Hoffmann, and Edward L. Dreizin,
"Combustion of Decane-based Slurries with Metallic Fuel Additives,"
The AIAA Region I Young Professional Student, Education Conference, Laurel, MD, November 2006.

To my parents, Teri and Josef, and to my grandmother, Maria

ACKNOWLEDGMENT

I would like to acknowledge and express gratitude towards my thesis advisor Dr. Edward L. Dreizin. I am indebted to his patience, guidance, experience, motivation, and insight which made my research possible. Special thanks are given to Dr. Boris Khusid and Dr. Mirko Schoenitz for participating in my committee and providing valuable feedback. I would also like to acknowledge the members of the Energetics Materials Laboratory, for their support of my research. Special thanks to Dr. Mikhaylo Trunov for his help with the numerical model.

TABLE OF CONTENTS

LIST OF TABLES

LIST OF FIGURES

LIST OF FIGURES
(Continued)

CHAPTER 1

INTRODUCTION

1.1 Objectives

The goal of this work is twofold. First, an understanding of electrostatic discharge sensitivity as related to the ignition of powders is to be established. A numerical model will be developed for the heat transfer in a powder bed subject to ESD sparking. The numerical model will be developed and calibrated considering properties of spherical Mg powder. This powder is selected as a benchmark material because of its well established properties and thermal ignition kinetics. A connection will be made as to whether ESD causes ignition by the thermal initiation of metal powders. The numerical model solutions will be compared to experimental results based on current testing methodology. The second goal of this work is to conduct experimental analysis of the ignition of powders using ESD as the ignition trigger. Parametric work will be conducted to determine the effect of electrode materials, capacitance and polarity and will provide a baseline to measurements in which ESD ignition sensitivity of different materials will be studied. Optical measurements will be taken of the ignition of Mg from which temporal and energetic characteristics of ignition will be determined. This paper presents the initial effort aimed to achieve the goals stated above.

1.2 Background

The current standards, such as MIL STD-1751A by which the ESD testing is performed today came about through an effort in the 1940s by the US Bureau of Mines to test the

hazards of explosives by electrical sparks [1]. In such a test apparatus, a moving electrode needle discharged a spark upon approaching the surface of the material. If some minimum threshold energy delivered to the powder caused a self-sustaining chemical reaction, ignition would occur. The potential energy based on the capacitance of stored charge delivered to the pin electrode and the potential difference between the electrodes offered a qualitative ranking of powder sensitivities. However the results of these tests may be misleading and a number of issues need to be addressed before a reliable and useful ranking for new reactive materials can be obtained.

There are two generic sets of issues that need to be addressed. The first set of issues has to do with the testing procedure itself. Related test procedures for the ESD sensitivity of gas mixtures have been well developed and documented [2-3]. It has been established that the material and shape of the electrodes, the discharge duration, the presence of moisture, and other parameters affect the ESD sensitivity substantially [2]. However, no comparable studies are available for ESD sensitivity testing of powder-like materials. In the current testing standards, there is no clear guidance regarding the environmental factors that need to be considered, which could either accelerate or mitigate ignition. There is also no detailed description for the shape and material of the high-voltage electrode. The pin electrode used to transfer the stored charge from the capacitor to the test surface is important in how the discharge is delivered to the surface. The pin shape affects the point of contact where the discharge will strike and it is vital to have a consistent shape for repeatable results. Also pin material affects how the discharge energy is transferred through the pin. For instance it has been reported that for high energies for nickel coated brass pins which are typically used, the coating was vaporized

which in turn reduced the discharge energy due to heat losses [1]. The current standards do not specify the discharge duration, which can make it difficult to make meaningful comparisons between different powders. In particular, the powder electric conductivity would affect the time constant of the capacitor discharge, so that different discharge durations can occur for different powders tested using the same experimental setup.

The second set of issues is unique to properties of powder-like energetic materials. For example, there is also little to no guidance regarding the experimental pressure or sample confinement. In testing of propellants, pressure can affect internal mechanical stresses which in turn affects ignition [4]. Confinement of the powder being tested can be crucial as well. For example, it was reported that metal powders exhibit a greater ESD ignition sensitivity being unconfined while black powder is more sensitive under confinement [1]. In addition to the issues common for all powders, reactive nanocomposite materials pose additional challenges. Their inherently heterogeneous structure with extremely developed reactive interface area can result in unusual thermal, mechanical, and electric properties, all of which affect their ESD sensitivity. Some of the related heterogeneous processes have recently been considered while modeling flame propagation for self-propagating high-temperature synthesis (SHS) [5] and similar considerations are necessary for analysis of the ESD sensitivity.

CHAPTER 2

ELECTROSTATIC DISCHARGE EXPERIMENT

2.1 Experimental Apparatus

A schematic diagram of the experimental setup is shown in Figure 2.1. ESD testing in accordance with the MIL-STD 1751A standard was performed using a Model 931 Firing Test System (FTS) by Electro-Tech Systems, Inc. Free metallic powder was placed into a stainless steel cup 15mm in diameter and 3mm in depth which was affixed to a grounded base. FTS includes a capacitor bank with capacitance varied in the range of 100pF to 10000pF which can be discharged through the spark gap directly or through an additional resistor varied from 50 to 5000Ω. The discharge pulse voltage that can be produced by the apparatus varies from 100V to 26kV.

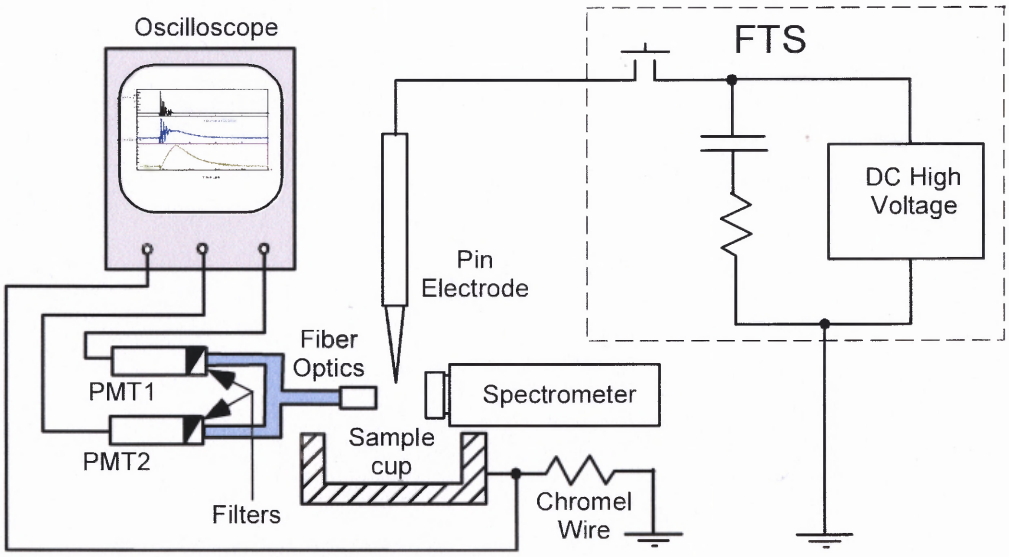

Figure 2.1 Schematic diagram of the experimental setup.

A short Chromel wire was used to ground the sample cup and the voltage drop measured across it was used to determine the spark current. A LeCroy WaveSurfer 64Xs Series oscilloscope was used to acquire and record signal traces.

Optical emission sources from a test were acquired using a fiber optics cable with a single window which branched off to multiple outputs. From the outputs, optical traces of the spark and oxidation of Mg emissions were acquired at two selected wavelengths by

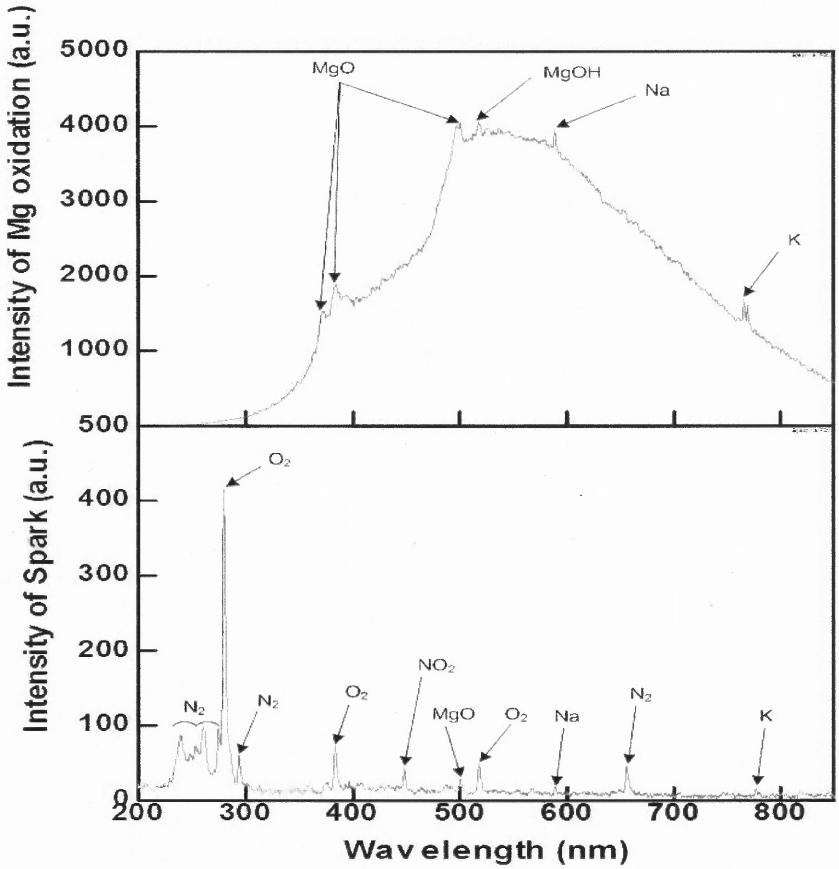

Figure 2.2 Emission spectra of the sparks between the pin electrode and empty sample cup (top) and between the pin electrode and igniting Mg powder (bottom).

two photomultiplier tubes by Hamamatsu Corp. and recorded by the oscilloscope. The choice of the bandpass interference filters for the optical traces was determined based on two initially measured optical spectra produced respectively by sparks between the pin

electrode and an empty cup and between the pin electrode and igniting Mg powder. The spectra were recorded using an EPP2000 spectrometer by Stellarnet Inc. and are shown in Figure 2.2. Main characteristic peaks are labeled based on the references [6] and [7]. It was observed that the spark produced between the pin electrode and an empty cup emitted primarily in the ultraviolet range and respectively, a 280nm filter by Cheshire Optics was used to detect the spark emission. Alternatively, the spectrum of the igniting Mg powder exhibited a strong and broad peak in the range of 500–600nm with an additional characteristic MgO peak prominent at 500nm. Therefore, a 500nm filter by Edmund Industrial Optics was used to filter the light produced by the igniting powder.

2.2 Current Calibration

A calibration of the discharge setup was conducted in order to collect meaningful traces for ESD ignition of a test powder. In particular the following was determined from the calibration: the value and reproducibility of the resistance, across which the oscilloscope trace was measured, and the value of any additional parasitic resistance and parasitic capacitance associated with each specific capacitor. In addition, the potential energy stored in each capacitor was compared to the energy delivered in the respective discharge.

Figure 2.3 is an equivalent circuit diagram of the discharge setup containing the added series resistors. The following capacitance and resistances are: C_A is the capacitance selected to produce the discharge, C_P is the parasitic capacitance, C_{man} is the manufacturer's defined parasitic resistance, R_B is the bleeder resistance, R_A is the resistance selected to model the resistance through which the discharge passes through

(i.e., human body model), R_S is the resistor used to shunt the spark gap, R_P is the parasitic resistance and R_I is the resistance over which the oscilloscope trace is measured.

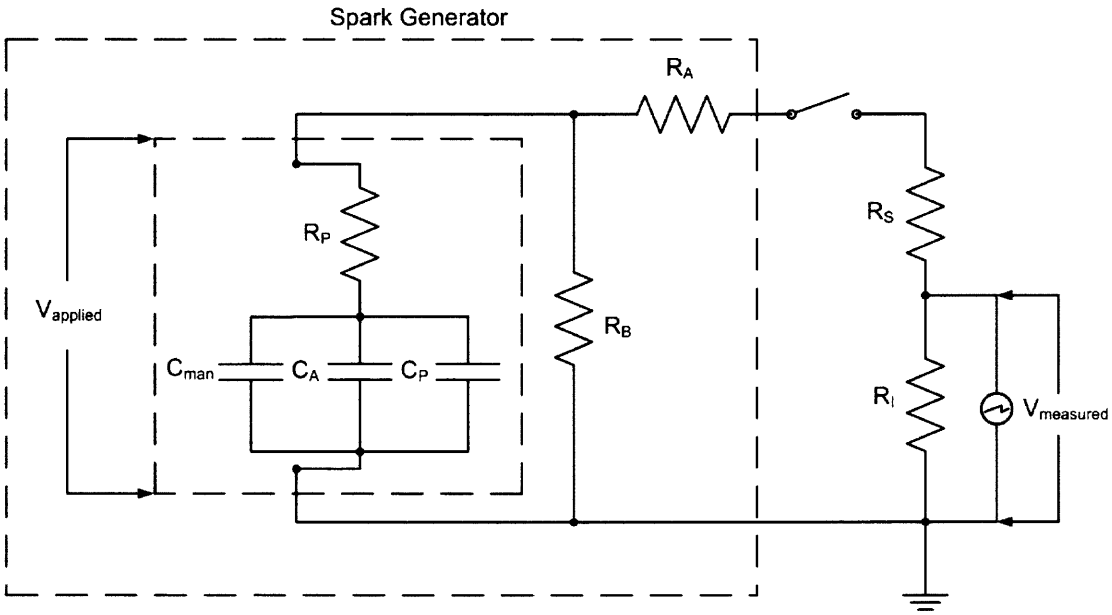

Figure 2.3 Equivalent circuit diagram used in determining total capacitance and total resistance.

To conduct the calibration, a known resistance was used to shunt the spark gap. This was achieved by soldering resistors to a copper wire, one end placed in the recess of the pin holder and the other end was connected to the same terminal as the wire used in measuring the current traces between the sample cup and Chromel wire resistor shown in Figure 2.1. Two resistors were placed in series for measuring current for the 10000pF and 5000pF capacitors. An ohm meter was used to measure actual resistance. The measured resistance of the two resistors was 420Ω. Three resistors were placed in series for measuring current for the 2000pF, 1000pF, 500pF, 250pF, and 100pF capacitors because current decay could not be measured with 420Ω. The measured resistance of the three resistors was 656Ω. The Chromel wire used to measure the current trace was 4.57cm long and was made of four tightly twisted 24 gauge Chromel wires. The equivalent resistance

was determined by treating the individual wires as parallel resistors, where the resistance provided by the manufacturer per length was 1.671Ω/ft [8]. The calculated resistance across the twisted Chromel wires was 62.7mΩ. Nominal and actual resistances measured by the ohm-meter R_A are given in Table 2.1.

Table 2.1 Summary of Nominal and Measured Resistances, R_A

Nominal Resistance R_A (Ω)	0	500	1500	5000
Measured Resistance R_A (Ω)	0.01	498	1555	4840

The voltage is applied over the selected capacitor C_A. To determine current, voltage is measured across R_I. Once the capacitance and voltage are set the switch is closed, which allows for current to pass over R_I and for a voltage trace to be acquired. The measured voltage trace compared with a calculated one:

$$V_{measured}(t) = \frac{V_{applied} \cdot R_I}{R_{Tot}} \cdot \exp\left(-\frac{t}{\tau}\right) \tag{2.1}$$

where t is time, R_{Tot} is the total resistance in series, τ is the time constant:

$$\tau = R_{Tot} \cdot C_{Tot} \tag{2.2}$$

where C_{Tot} is the total capacitance in series. R_{Tot} and C_{Tot} are:

$$R_{Tot} = R_A + R_S + R_P + R_I \tag{2.3}$$

$$C_{Tot} = C_A + C_{man} + C_P \tag{2.4}$$

where C_{man} is the manufacturer defined parasitic capacitance which is 55pF. In order to match experimental and calculated voltage traces values of R_P and C_P were used as adjustable parameters. A comparison was conducted between the potential energy of the discharge and actual energy delivered by the discharge. The potential energy of the discharge is:

$$PE = \frac{1}{2} C_{Tot} \cdot V_{applied}^2 \tag{2.5}$$

and the measured energy is:

$$ME = \sum_{0}^{n} \left(\frac{V_{measured}}{R_I} \right)^2 \cdot R_{Tot} \cdot \Delta t \tag{2.6}$$

where n is the total number of data points of a voltage trace and Δt is the time step between data points which is 40ns. For the purposes of curve fitting, a 95% confidence interval was used to achieve a fit. Also, the manufacturer defined a ±10% tolerance on the value of the applied capacitance. The applied capacitance, C_A, was therefore adjusted to achieve a better fit as needed. A curve fit was optimized by minimizing the percent error between measured and potential energies while decreasing the parasitic resistance while keeping it a real resistance. This was done by decreasing the applied capacitance in increments of 5pF until the fit was optimized as mentioned. Curve fitting, where R_P, C_P, and R_I were adjustable parameters, was performed with the same C_A with combinations of applied voltage, and R_A. Table 2.2 shows the nominal value and actual value of C_A used to achieve a reasonable curve fit. The capacitance value for the 250pF capacitor exceeded the minimum tolerance because otherwise an unrealistic parasitic resistance was obtained. Figure 2.4 shows a typical current measurement and its fit.

Table 2.2 Summary of Nominal and Actual Capacitance, C_A, used in Fitting

Nominal C_A (pF)	10000	5000	2000	1000	500	250	100
Used C_A (pF)	10000	5000	2000	960	500	180	100

Table 2.3 contains the following results from curve fitting: nominal capacitance (C_A), voltage (V), and resistance (R_A), as well as resistance across the wire (R_I), parasitic resistance associated with a capacitor (R_P), potential energy (PE), measured energy from measured voltage (ME), and percent error between potential and measured energies (Err).

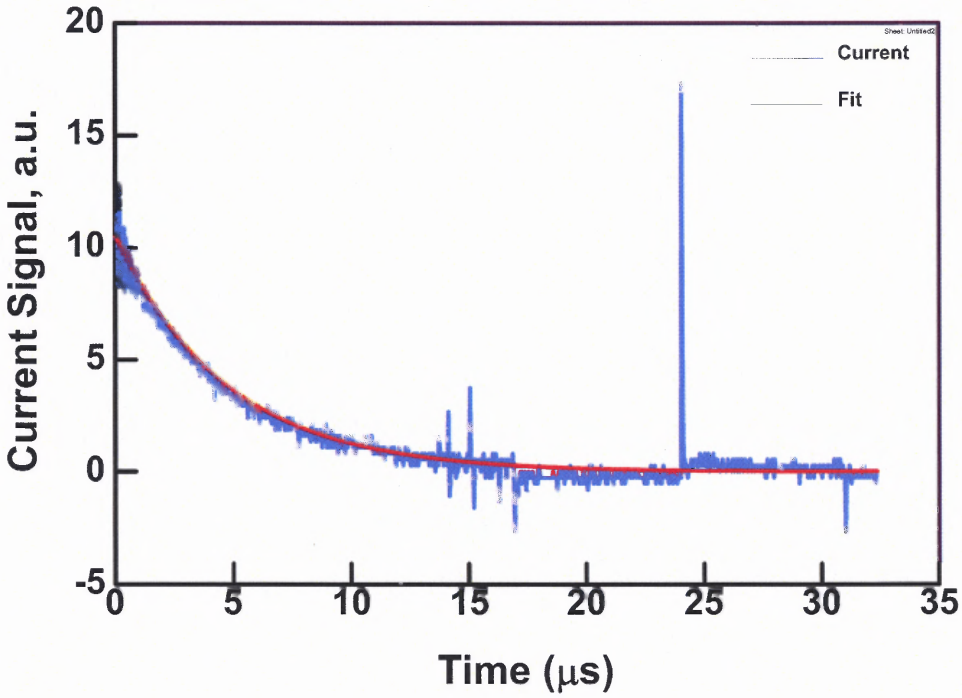

Figure 2.4 Typical current trace and fit used in determining time constant (current trace was produced with 5kV, 10000pF, and 0Ω).

It was not possible to obtain C_P because reasonable fits and realistic R_P and R_I could not be obtained. Therefore C_P was forced to be zero, and reasonable fitting was then achieved. The average wire resistance value is 60.1mΩ±10.3mΩ. Low parasitic resistances and small errors were obtained for the 10000pF, 5000pF, 2000pF, and 1000pF capacitors. For the 500pF and 100pF capacitors the parasitic resistances are high and for the 250pF capacitor the error is large as compared to the other capacitors.

Table 2.3 Summary of Nominal Values used in Curve Fitting and Obtained Wire Resistance, Parasitic Resistance, Potential Energy, Measured Energy, and Error Between the Potential and Measured Energies

C_A (pF)	$V_{applied}$ (kV)	R_A (Ω)	R_I (mΩ)	R_P (Ω)	PE (J)	ME (J)	Err (%)
10000	5	0	59.2	49.2	0.126	0.127	0.8
10000	5	500	59.2	49.2	0.126	0.126	0
10000	10	500	59.2	49.2	0.503	0.504	0.
5000	5	0	44.1	23.6	0.0632	0.0643	1.7
5000	5	500	44.1	23.6	0.0632	0.0636	0.6
5000	10	500	44.1	23.6	0.253	0.254	0.4
2000	10	1500	59.1	120	0.103	0.103	0
2000	10	5000	59.1	120	0.103	0.103	0
2000	15	5000	59.1	120	0.231	0.231	0
1000	15	1500	54.1	2.20	0.119	0.116	2.5
1000	15	5000	54.1	2.20	0.119	0.114	4.2
1000	20	5000	54.1	2.20	0.211	0.203	3.8
500	20	1500	76.4	3620	0.111	0.112	0.9
500	20	5000	76.4	3620	0.111	0.112	0.9
500	25	5000	76.4	3620	0.173	0.175	1.2
250	15	5000	68.7	99.6	0.0343	0.0272	21
250	20	5000	68.7	99.6	0.0610	0.0484	21
100	20	5000	59.7	5010	0.0310	0.0318	2.6
100	25	5000	59.7	5010	0.0484	0.0496	2.6

The average wire resistance value of 60.1mΩ was comparable to the 62.7mΩ calculated. The cause of the high parasitic resistance of the 500pF and 100pF capacitors may be attributed to complex impedance. The error of the 250pF capacitor is most likely the actual capacitance is smaller and outside the given tolerance. The total values of resistance, capacitance, and applied voltage will be used in the numerical model to describe the current of the spark applied to a powder bed.

2.3 Optical Traces Calibration

UV (280nm) and green (500nm) traces were acquired for a spark striking a metal substrate. Figure 2.5 shows a typical example of current, UV and green filtered traces.

The current and UV filtered trace showed noticeable oscillations corresponding to the quick charging and discharging of the capacitor producing the spark. The green filtered trace showed no oscillation but a well defined peak which corresponds to the heating and cooling of the metal substrate. Generally, the UV filtered traces are distinctly different from the green filtered traces. Traces were obtained for the following discharge configurations: aluminum and stainless steel substrates, positive and negative polarity, and 1000pF, 2000pF, 5000pF, and 10000pF capacitors. For each specific discharge configuration, the UV and green filtered traces were acquired along with the current trace and each experiment was repeated five times. The applied voltage and resistance, R_A used were 5kV and 0Ω, respectively.

Figure 2.6 shows measurements obtained from a typical UV trace. For a periodic oscillation pattern, the first amplitude, last amplitude, and period of oscillations were measured. The time period of oscillations could also be obtained from the current trace, closely correlated with the UV filtered trace. Figure 2.7 shows the average period of amplitudes for the capacitors, substrates, and polarity combinations mentioned. The average period of amplitudes increases with increasing capacitance due to the longer time needed to charge and discharge a capacitor.

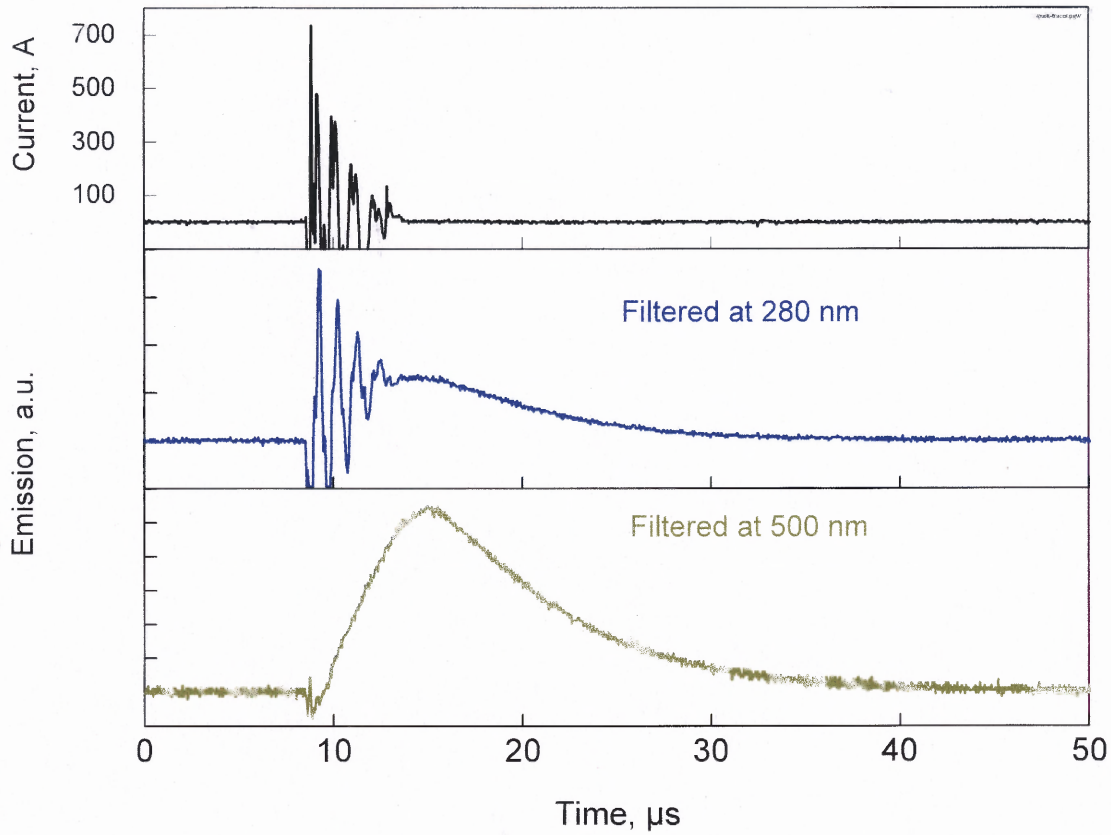

Figure 2.5 Example of current and optical traces (traces were obtained from spark striking a stainless steel substrate, negative polarity, 5kV, 5000pF, and 0Ω).

Figure 2.8 shows measurements obtained from a typical green trace. The time period between the spark to the peak on the green trace and the time of green peak decay to 1/10 its value are measured. Figure 2.9 shows the time periods of increase and decay for the capacitors, substrates, and polarity combinations mentioned. The time period between the spark and the green peak increased with increasing capacitance due to the increased energy deposited to the substrate surface at higher capacitance.

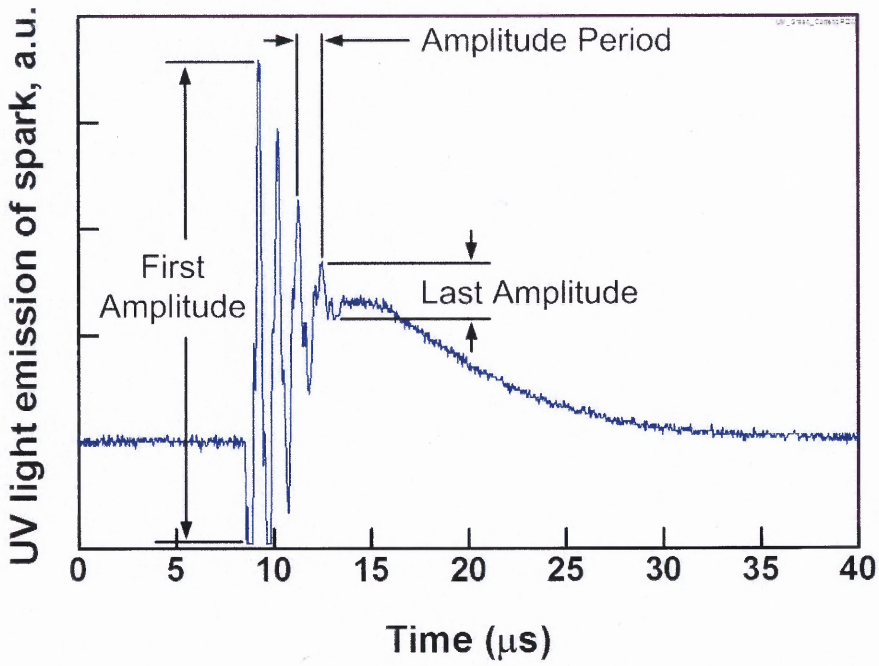

Figure 2.6 First amplitude, last amplitude, and oscillation period measured from UV signal.

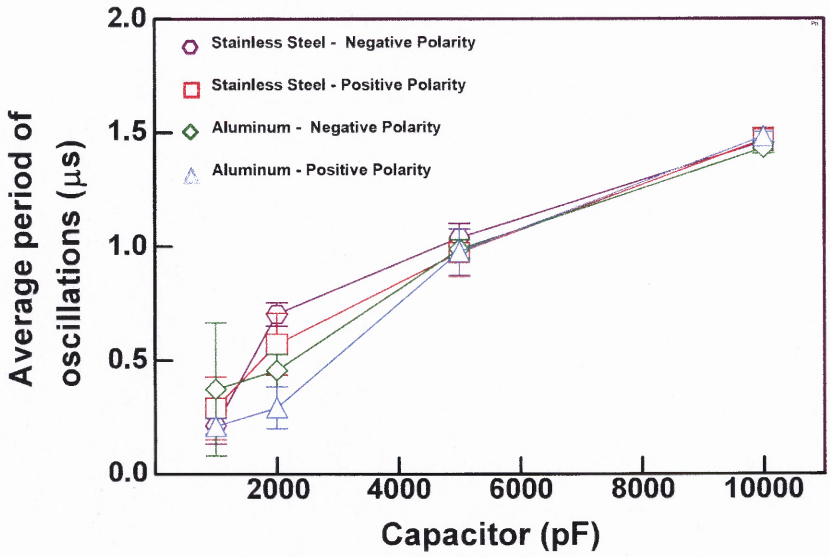

Figure 2.7 Average period of oscillations obtained from the UV signal (for 1000pF, 2000pF, 5000pF, 10000pF capacitance, for aluminum and stainless steel substrates, and positive and negative polarities).

This time period also increases with increased capacitance due to the longer time needed to cool when higher energy was deposited to the substrate. The aluminum substrates cool faster than the stainless steel substrates for the 5000pF and 10000pF capacitors which is attributed to aluminum having higher thermal conductivity and thermal diffusivity. In general the trends are reasonable and qualitatively understood. No marked effect of polarity was observed, and all subsequent experiments will use positive polarity.

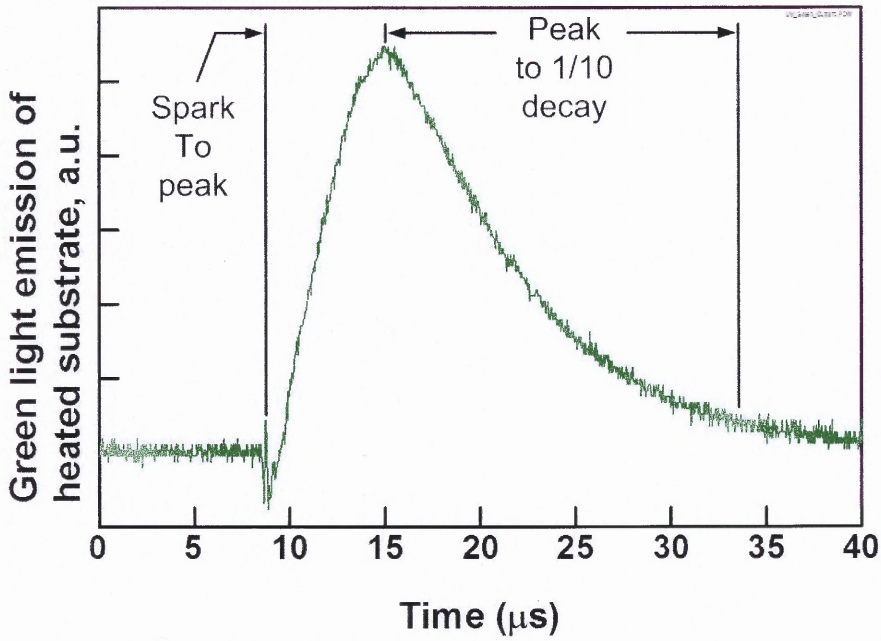

Figure 2.8 Oscillation start (spark) on UV signal to peak on green signal, and peak to 1/10 peak decay on green signal measured from green signal.

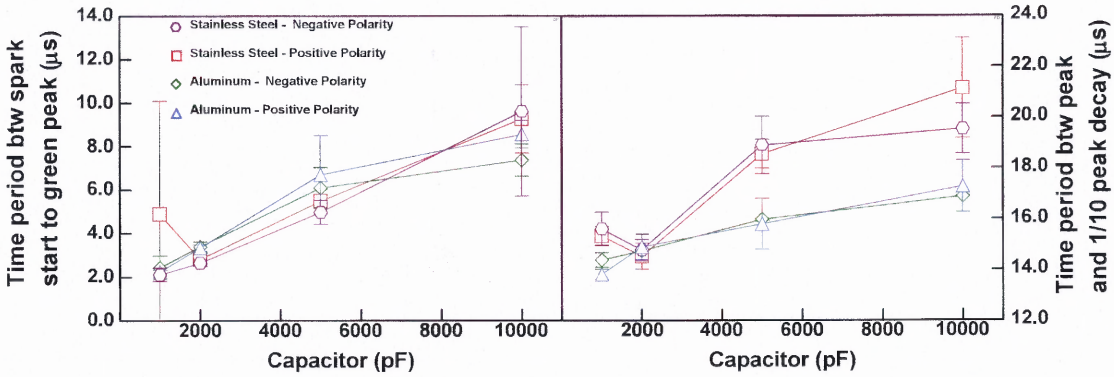

Figure 2.9 Time period between oscillation start to green peak and time period between green peak and 1/10 peak decay (for 1000pF, 2000pF, 5000pF, 10000pF capacitance, for aluminum and stainless steel substrates, and positive and negative polarities).

2.4 Mg Ignition Experiments

These experiments were designed to analyze the validity of the proposed model of energy transfer from the spark to the powder bed. Initial ignition tests by spark showed that a portion of the powder is ejected from the cup for both ignition and non-ignition cases. The ejection was attributed to the effect of the spark shock wave [9]. In order to match the heat transfer model which does not take into account any mass transfer of the powder, a small amount of binder was added to the powder. The binder was Star Brite liquid electric tape and consisted of a vinyl acetate copolymer, ketones, and other hydrocarbons. In order to maintain the same cylindrical geometry of free powder and the model, the binder, powder, and acetone was mixed together to form a slurry that could be poured into the electrode cup. The mass percent of the solid portion of binder was determined by allowing a small amount of binder to air dry on a balance then recording the weight which is the solid portion of the binder remaining. The mass percent of the solid portion was 0.42. A solution of acetone and binder was prepared by weighing out 0.1g of binder

and adding 10mL of acetone. From the binder/acetone solution 1mL was added to 0.4g of powder to produce the slurry mixture which is well stirred and then poured into the cup. The solid portion of the binder was 0.3 weight percent of the entire powder/binder composition, and was determined from the densities of Star Brite liquid electric tape, acetone, and Mg [10-12]. The binder amount was chosen because the amount was the minimum weight of binder needed to prevent powder ejection.

A special electrode cup was manufactured for these experiments in order to enable the energy transfer analysis with simplified boundary conditions. The electrode cup was made by gluing a plastic washer to an aluminum substrate. The electrode cup and its respective dimensions are shown in Figure 2.10. The small thickness of the washer facilitates maintaining an even powder surface. More slurry is added than needed to guarantee that powder occupies the entire volume. Once the hydrocarbons and ketones have mostly evaporated the excess powder is scraped off leaving a flat surface.

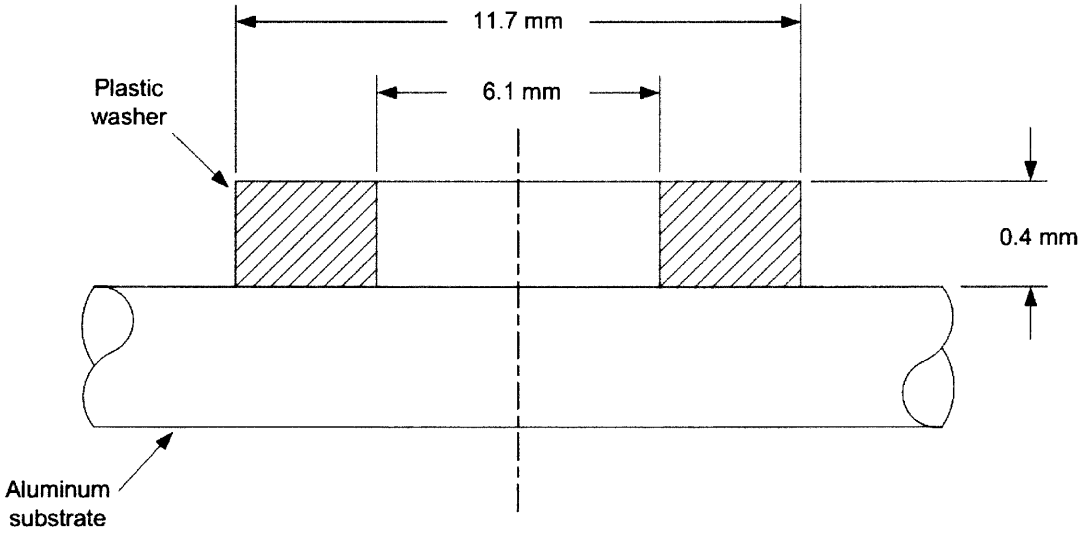

Figure 2.10 The electrode cup prepared for Mg ignition tests.

Once the sample is prepared, the ignition tests follow. Prior to the measurements described below, minimum ignition energy (MIE) was experimentally determined for the Mg samples using sparks generated by different capacitors. The voltages corresponding to MIE for each capacitor are listed in Table 2.4

Table 2.4 Summary of Capacitances, C_A, Applied Voltage and Minimum Ignition Energy

C_A (pF)	1000	2000	5000	10000
Voltage (kV)	8	5	3	2.5
MIE (mJ)	34	26	23	31

A series of tests were run to observe the ignition delay as a function of capacitance and voltage. The first test was run at the MIE of Mg at 1000pF, 2000pF, 5000pF, and 10000pF to observe if duration of the spark has an effect on ignition. Secondly, ignition tests were run to observe the effect of varying discharge energy at a particular capacitor setting by varying the voltage between the pin and cup electrodes. In all runs, the pin tip to powder surface spacing was 0.2mm and the applied resistance selected was 0Ω. Also for each capacitor and voltage combination, a total of ten repetitions were conducted.

CHAPTER 3

HEAT TRANSFER MODEL

A numerical heat transfer model was created for studying ignition by ESD. The powder is contained in a cylindrical cup electrode. The domain in which the heat transfer is analyzed is a disk with elements taking the shape of a series of inserted and stacked rings with central cylindrical elements, as illustrated in Figure 3.1. The element's vertical dimension is z_m and the element radius is r_n. The indices m and n were introduced to number ring-shaped elements expanding in the stacked direction vertically, and radially, respectively.

For each element, the heat transfer equation is considered (with indices m,n removed for brevity) as:

$$\rho VC\frac{T(t+\Delta t)-T(t)}{\Delta t}=\dot{Q}_{Cond}+\dot{Q}_{Conv}+\dot{Q}_{Rad}+\dot{Q}_{Disch}+\dot{Q}_{Joule}+\dot{Q}_{Chem} \tag{3.1}$$

where, ρ is density, V is volume, C is specific heat, T is temperature, t is time, Δt is the time step and $\dot{Q}_i$ are different heat transfer rate terms. For each control element, the external and internal radii were introduced as r_n and r_{n-1}, as shown in Figure 3.1. For the central stack of cylindrical elements, n=1 and r_{n-1}=0 and the volume of each control element was computed as $V_{m,n}=\pi z_m\left(r_n^2-r_{n-1}^2\right)$. The conductive heat transfer rate, in general, included two axial (top and bottom) and two radial (internal and external) contributions, which were computed as:

$$\dot{Q}_{Cond} = k_{m+1,n} A_{bot}^{axi} \frac{T_{m+1,n} - T_{m,n}}{z_m} + k_{m-1,n} A_{top}^{axi} \frac{T_{m-1,n} - T_{m,n}}{z_m} + k_{m,n+1} A_{ext}^{rad} \frac{T_{m,n+1} - T_{m,n}}{r_{n+1} - r_n} + k_{m,n-1} A_{in}^{rad} \frac{T_{m,n-1} - T_{m,n}}{r_n - r_{n-1}} \tag{3.2}$$

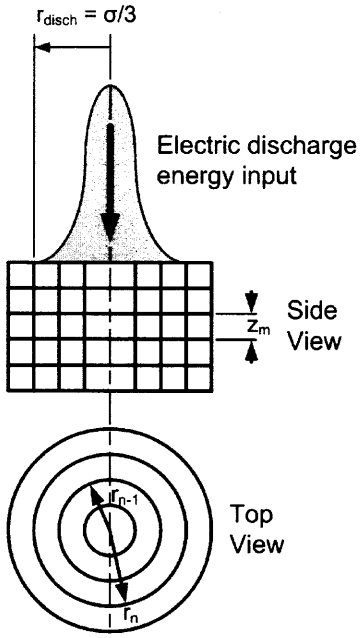

Figure 3.1 Geometry of the computational domain.

where $k_{m+1,n}$, $k_{m-1,n}$, $k_{m,n+1}$, and $k_{m,n-1}$ are the thermal conductivities of a specific control volume at the bottom, top, exterior, and interior surfaces. A_{bot}^{axi}, A_{top}^{axi}, A_{ext}^{rad}, and A_{in}^{rad} are the bottom, top, exterior, and interior areas respectively. They are calculated as:

$$A_{bot}^{axi} = A_{top}^{axi} = \pi\left(r_n^2 - r_{n-1}^2\right) \text{ and } A_{ext}^{rad} = 2\pi r_n z_m \text{ and } A_{in}^{rad} = 2\pi r_{n-1} z_m \tag{3.3}$$

For the top layer elements, there is only bottom axial contribution to this heat transfer term. For the elements at the boundaries, the boundary temperature is assumed to be equal to the room temperature. For the central stack of cylindrical elements, there is only one radial contribution (external) and the external radius of the cylinder is used to calculate the surface areas. The thermal conductivity of the powder bed is determined

using a laser flash technique [13]. It is primarily determined by the thermal resistance of the particle-particle contacts while the thermal resistance of the bulk material (magnesium) is small. Therefore, the control volume element dimensions can be considered comparable to the size of the particle. This way, the temperature within each particle equilibrates nearly instantaneously, while the rate of conductive heat transfer between the particles is relatively low. This rate changes rapidly when the particles experience phase changes, such as melting and boiling. In this initial model, the thermal contact resistance changes when the particles are completely molten. In this model, it is assumed that the thermal conductivities of all the control volume elements adjacent to the molten element become equal to that of bulk Mg. Thus, if a control element m,n is molten, for the remaining elements that exist m-1,n; m+1,n; m,n-1; and m,n+1, the value of k is adjusted.

To consider melting and boiling in the context of the heat transfer balance analysis, the gravimetric enthalpies of melting H_{melt} and boiling, H_{boil}, are introduced. Once the melting temperature is reached for an element, its temperature is not allowed to increase above the melting point until the following equation is met:

$$\sum_{i,j} \dot{Q}_i \Delta t_j \geq \rho V_{m,n} H_{melt} \tag{3.4}$$

where index i indicates the summation over all the heat transfer rate terms and index j shows summation over a range of time steps during melting. As noted above, the thermal conductivities of the control elements adjacent to the molten one are adjusted to account for an enhanced heat transfer. Boiling is considered in a similar fashion. Once the boiling temperature is reached for an element, its temperature is not allowed to increase above the boiling point until the following equation is met.

$$\sum_{i,j} \dot{Q}_i \Delta t_j \geq \rho V_{m,n} H_{boil} \tag{3.5}$$

Once the element is boiled off, the adjacent element below is modified to account for convective heat transfer if exposed to the air.

The convective heat transfer term, $\dot{Q}_{Conv}$ is calculated only for the elements in the top layer or for elements that appear at the top when the layers above them evaporate. It is calculated assuming that convection occurs with ambient air at room temperature, T_∞ and that it can be described as natural convection over a flat plate. Furthermore, the characteristic dimension of the top plate was assumed to be equal to the area directly heated by the electric discharge. Therefore, the characteristic plate dimension was assumed to be equal to the radius of the discharge column (see details below), r_{disch}. Respective Rayleigh number, Ra, was calculated as [14]:

$$Ra = \frac{g\beta\left(T_\infty - T_{m,n}\right) r_{disch}^3 \Pr}{\nu^2} \tag{3.6}$$

where g, is the gravitational constant, $\beta = \frac{1}{T_{film}}$ is the coefficient of gas thermal expansion calculated assuming that air is an ideal gas at the film temperature $T_{film} = \frac{T_\infty + T_{m,n}}{2}$, Pr and ν are Prandtl number and the kinematic viscosity, respectively, both taken at the film temperature. Dimensionless heat transfer coefficient, or Nusselt number was then calculated as [14]:

$$Nu = 0.54 Ra^{0.25} \tag{3.7}$$

Finally, the convection heat transfer term was calculated as:

$$\dot{Q}_{Conv} = \frac{k_{air}}{r_{disch}} Nu \cdot A_m^{axi} \left(T_\infty - T_{m,n}\right) \tag{3.8}$$

where k_{air} is the thermal conductivity of air at the film temperature.

Similar to the convection term, the radiation term is also calculated for the top layer only or for the elements that appear at the top when the elements above them evaporate. The external wall surfaces also are assumed to be at room temperature, so:

$$\dot{Q}_{Rad} = \varepsilon\sigma A_m^{axi}\left(T_\infty^4 - T_{m,n}^4\right) \tag{3.9}$$

where ε is the emissivity of the powder and σ is Stefan-Boltzmann constant.

Joule heating was assumed to occur between the contacts between elements. To determine the heat deposited to each particle by Joule heating a resistor network was modeled to represent the contact resistances. Since actual electrical resistance of Mg was unknown either in the powder or liquid phases, it was assumed that the ratio of liquid to powder resistance to be the same as the ratio of powder and bulk thermal conductivities. Therefore the bulk electrical resistivity was assumed to be 3.3μΩ-cm and powder resistivity was assumed to be 579 times the bulk electrical resistivity which is the ratio of bulk to powder thermal conductivity [15]. For those neighboring elements for which at least one element had melted, the contact resistance was assumed to be the bulk resistance because of the surface contacts made by molten Mg. The contact resistance is:

$$R = \frac{\rho d}{A} \tag{3.10}$$

ρ is the contact resistivity, d is the center to center distance between elements in contact, and A is the surface area of elements that are in contact with each other. Figure 3.2 shows the resistors considered around each element. For an element, a single equation describes the net current determined by voltage on this and surrounding elements:

$$\frac{V_{m+1,n} - V_{m,n}}{R_{m+1,n\to m,n}} + \frac{V_{m-1,n} - V_{m,n}}{R_{m-1,n\to m,n}} + \frac{V_{m,n+1} - V_{m,n}}{R_{m,n+1\to m,n}} + \frac{V_{m,n-1} - V_{m,n}}{R_{m,n-1\to m,n}} = \mathrm{I}_{m,n} \tag{3.11}$$

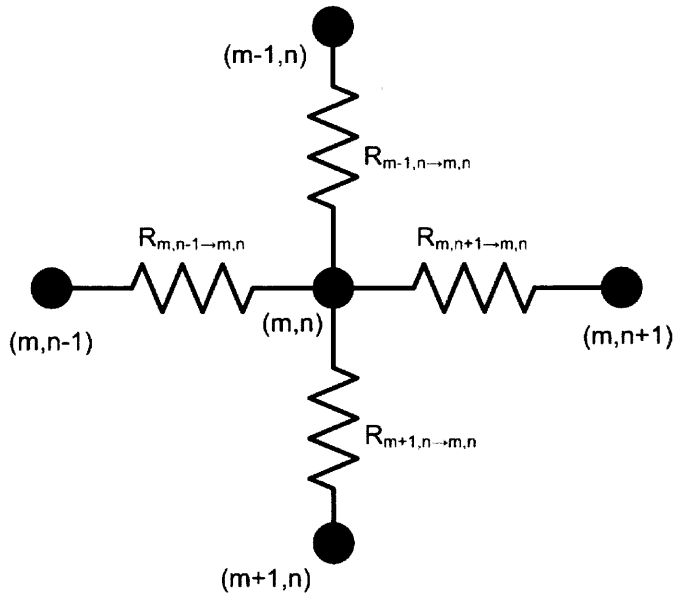

Figure 3.2 Resistor network about an element.

The voltage along the bottom surface and along the cup wall is grounded at 0V. These surfaces act as a current sink whereas the surface of discharge produced by the column contacting the powder bed is the current source. The voltage of each element is solved simultaneously from the net current entering each element and the contact resistances of all neighboring elements that exist. This is done by generating a set of matrices of all contact resistances, voltages, and net current. The matrix multiplication used to determine voltage is:

$$\begin{aligned} \left[\tfrac{1}{R}\right][V] &= [I] \\ [V] &= \left[\tfrac{1}{R}\right]^{-1}[I] \end{aligned} \tag{3.12}$$

The power dissipated across a contact resistance and heating adjacent particles is:

$$\dot{Q}_{Joule} = \frac{(\Delta V)^2}{2R} \tag{3.13}$$

ΔV is the voltage drop across the contact resistance, and R is the contact resistance. The half in Equation 3.13 accounts for the energy dissipated across the contact resistance being divided evenly between the two particles in contact. For the topmost elements exposed to the discharge the energy dissipated assuming zero resistance from the discharge is:

$$\dot{Q}_{Disch} = I_n^{\,2} R \tag{3.14}$$

The energy from the electric discharge was assumed to decay in time exponentially. The time constant of this decay, τ is determined by the characteristic of the respective electric circuit, $\tau = RC$, where R is the equivalent electrical resistance and C is the capacity of the high-voltage capacitor used to produce the electric discharge. It is assumed that the current density of the discharge is supplied to the surface of the powder as a revolved Gaussian distribution. Also, it is assumed that the elements not directly exposed to the spark have zero net current. The portion of current density which enters in an individual surface element is:

$$I_n = \frac{1}{\sigma^2 \pi} \int_{r_{n-1}}^{r_n} e^{\frac{-r^2}{\sigma^2}} 2\pi r dr \tag{3.15}$$

For calculations, the radius of discharge, $r_{Disch} = \sigma/3$ (Figure 3.1) can be varied adjusting the standard deviation σ of the Gaussian distribution. The current delivered during a single time step follows an exponential decay and is given as:

$$I(n,t) = I_n \frac{V_{applied}}{R_{Tot}} \cdot \exp\left(-\frac{t}{\tau}\right) \tag{3.16}$$

where τ is the time constant, and t actual time.

Finally, the term describing an exothermic reaction in the powder that can lead to the thermal runaway and self-sustaining reaction, $\dot{Q}_{Chem}$ was analyzed. For thermal ignition of metallic particles, this "chemical" heat transfer rate term is usually described using an Arrhenius function [16-17]:

$$\dot{Q}^{0}_{Chem} = V_{m,n} Z \cdot \Delta H \exp\left(-\frac{E_A}{RT_{m,n}}\right) \tag{3.17}$$

where ΔH is the volumetric enthalpy of oxidation, E_A is activation energy, Z is the pre-exponent, and R is the universal gas constant. This expression describes the heat release due to a heterogeneous reaction while the amounts of reactants are unlimited. The formalism is well suited for description of ignition of individual particles. The assumed oxygen profile for the reaction rate controlled by Equation 3.17, or for the so called "kinetic regime" of oxidation is shown on the top of Figure 3.3.

For metal particles, it is usually assumed that when a particle ignites, its temperature rapidly increases to the metal's boiling point and the reaction rate is no longer described by Equation 3.17. Instead, it can be limited by the kinetics of the vapor-phase reactions for very fine (typically, less than 1 μm) particles or by the rate of oxygen diffusion to the flame for particles of larger dimensions [18-19]. In the case considered here, it is expected that at least some particles will ignite and thus Equation 3.17 will stop being valid for describing their reaction rate. On the other hand, it is important to have a description of this heat transfer rate term valid even after ignition of some portion of the powder bed has occurred. This description may be critical for understanding the mechanisms of ignition in the powder bed. Because the dimensions of the entire bed are large, it is assumed that when a particle (or a specific control element) ignites, its reaction

rate will be limited by diffusion. A number of simplifying assumptions necessary to describe this situation approximately are made below.

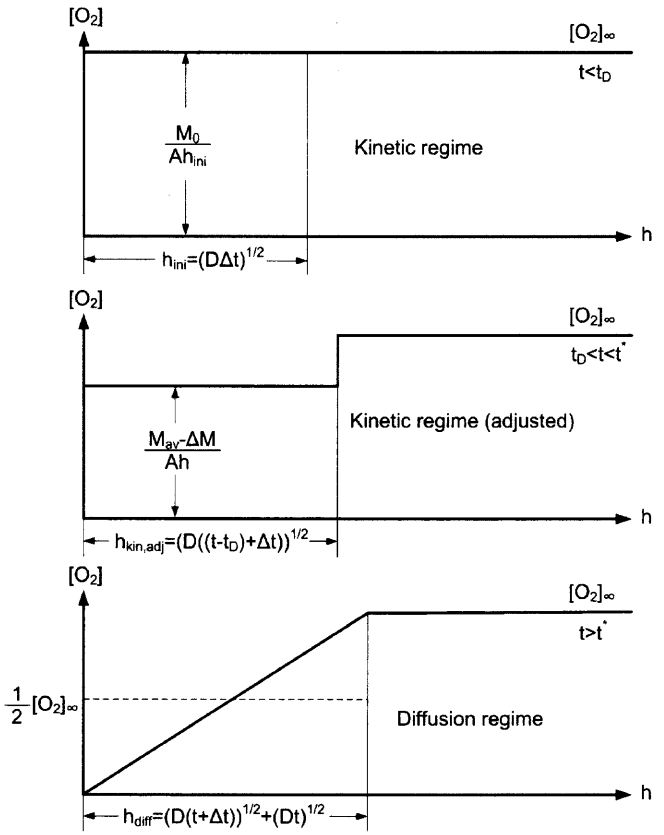

Figure 3.3 The chemical reaction for the kinetic regime (top) is described by Equation 3.17, the chemical reaction for the adjusted kinetic regime (center) is described by Equation 3.24, and chemical reaction for the diffusion regime (bottom) is described by Equation 3.26.

The number of moles of oxygen consumed as a result of reaction described by Equation 3.18 during a single time step, ΔM, is calculated as:

$$\Delta M = \frac{\dot{Q}^{0}_{Chem}}{\Delta H_{O_2}} \Delta t \tag{3.18}$$

where ΔH_{O_2} is the combustion enthalpy normalized per mole of O_2. The value of ΔM was compared to the total number of moles of oxygen available for reaction, M_0.

Initially, it was assumed that oxygen can be available from a gas layer above the powder bed with a thickness h_{ini} determined by the time step, Δt: $h_{ini} = \sqrt{D\Delta t}$, where D is the gas diffusion coefficient calculated as [20]:

$$D = 1.8 \times 10^{-5} \left(\frac{T_{film}}{273} \right)^{1.75} \left[\frac{m^2}{s} \right] \tag{3.19}$$

Thus, for each stack of control volume elements, the total number of moles of oxygen available for reaction during a single time step was estimated as:

$$M_0 = [O_2]_\infty A_m^{axi} h_{ini} \tag{3.20}$$

where $[O_2]_\infty$ is the concentration of oxygen in air. When the amount of oxygen consumed during a time step becomes a noticeable fraction of the oxygen available for the reaction, a first correction is introduced. The following equation was used to begin using the correction:

$$\frac{\sum_0^{t_D} \Delta M}{M_0} > X \tag{3.21}$$

where X<<1 is an arbitrarily selected constant that is chosen to be equal to 0.05 for the initial calculation. Before Equation 3.21 is satisfied, the effect of diffusion on the reaction rate is considered negligible and the heat transfer term $\dot{Q}_{Chem} = \dot{Q}^0_{Chem}$. It is also assumed that the chemical reaction can occur in any layer of the powder bed, e.g., the diffusion resistance of the porous powder bed to oxygen is neglected. After Equation 3.21 is satisfied, it is assumed that diffusion started to play a noticeable role in limiting the rate of chemical reaction. The chemical reaction is now only allowed in the top layer of the powder bed, which is exposed to the ambient gas directly. A layer of finite

thickness, h, is considered from which oxygen can reach the sample surface. This layer is introduced after a specific time t_D, corresponding to the time when Equation 3.21 is satisfied. For all times $t>t_D$, the total number of moles of oxygen available for reaction is computed as:

$$M_{av} = [O_2]_\infty A_{top}^{axi} h = [O_2]_\infty A_m^{axi} \sqrt{D\left((t - t_D) + \Delta t\right)} \tag{3.22}$$

In other words, the thickness of the layer of diffusion influence, h, or the layer from which the oxygen available for reaction can diffuse to the reacting surface is calculated to increase in time. At the same time, a decrease in the oxygen concentration at the surface of the sample is estimated. The estimate assumes a linear oxygen concentration profile in the zone of diffusion influence, so that:

$$[O_2](t) = \frac{M_{av} - \sum_0^t \Delta M_j}{A_{top}^{axi} \cdot h} \tag{3.23}$$

where for each new time step, the values of ΔM are calculated considering the values of $\dot{Q}_{Chem}$ calculated for the previous time step. The heat transfer rate term $\dot{Q}_{Chem}$ for each time step after $t>t_D$ is calculated using the Arrhenius Equation 3.24 with a corrected pre-exponent:

$$\dot{Q}_{Chem} = V_{m,n} Z \cdot \Delta H \frac{[O_2](t)}{[O_2]_\infty} \exp\left(-\frac{E_A}{RT_{m,n}}\right) \tag{3.24}$$

Finally, at some time t^*, the oxygen concentration in the vicinity of the sample becomes half of the original $[O_2]_\infty$. After that time, the reaction rate is governed by diffusion of oxygen and the available number of moles of O_2 consumed during a time step, Δt is estimated as:

$$\Delta M(t) = \frac{1}{2} A_{top}^{axi} \left[\sqrt{D(t+\Delta t)} - \sqrt{Dt} \right] [O_2]_\infty \tag{3.25}$$

Based on the consumption of O_2 based on Equation 3.25, the heat transfer rate term $\dot{Q}_{Chem}$ is defined as:

$$\dot{Q}_{Chem} = \frac{\Delta M(t) \cdot \Delta H_{O_2}}{\Delta t} \tag{3.26}$$

Figure 3.4 shows schematically assumed oxygen concentration profiles for each of the described calculation algorithms.

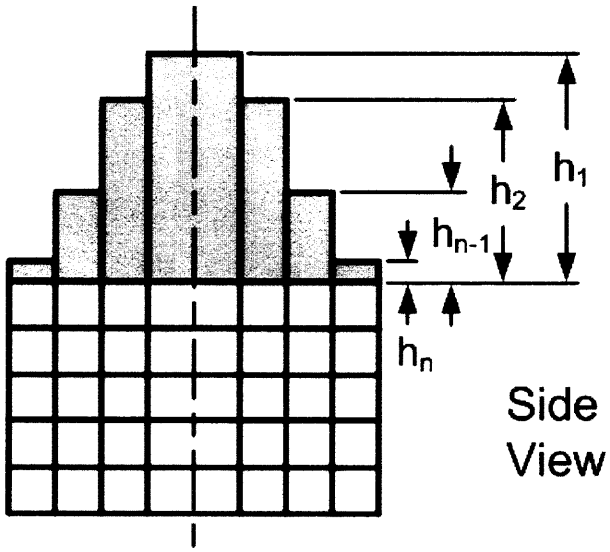

Figure 3.4 Diffusion volumes over their respective volumes formed by a specific time t. The diffusion volumes are greater for elements that have started to consume oxygen (i.e., for which reaction described by Equation 3.17 became significant) earlier in time.

To accelerate the computations, an adaptive time step is used. When the temperature increase in a control element over a single time step exceeds a pre-selected threshold value, the time step is reduced by a factor of two and the calculation is repeated. When the threshold value is not exceeded, the time step is allowed to increase for the following calculation cycle. The specific procedure for increasing the time step is

based on the computed maximum temperature increase $\Delta T_{m,n}^{\max}$ in a single control volume. This increase is compared to the pre-selected threshold value, ΔT_0 and a characteristic temperature difference for the specific time step, ΔT_{step} is calculated as:

$$\Delta T_{step} = \frac{\Delta T_{m,n}^{\max} - \Delta T_0}{\Delta T_0} \tag{3.27}$$

The factor by which the time step for the next cycle of calculation is increased is directly proportional to this value.

CHAPTER 4

RESULTS AND DISCUSSION

4.1 Mg Ignition Observations

Following MIL-STD 1751A, a load of 50mg of powder was placed into the electrode cup. When the specified energy was discharged to the powder surface, ignition occurred if some energy threshold was reached or exceeded for a particular powder being tested. Figure 4.1 shows three electrode cups containing Mg powder, where the cup diameter is 15mm.

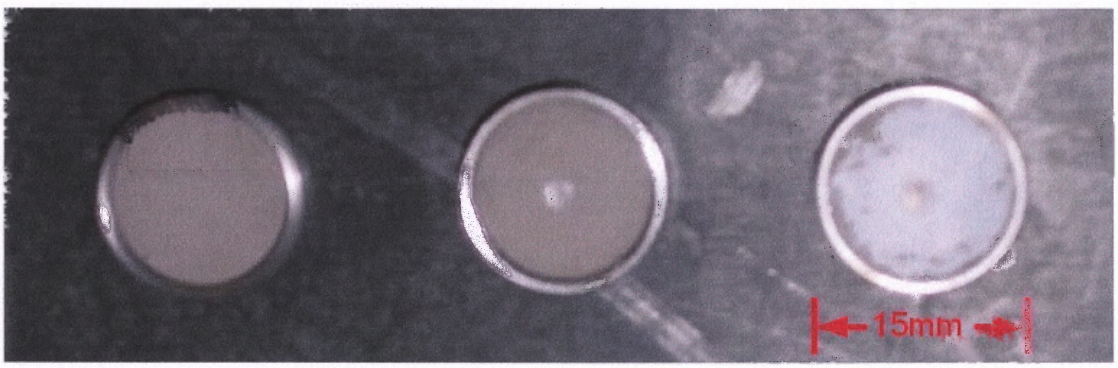

Figure 4.1 Electrode cups containing Mg powder; left cup contains powder that has not been struck by a spark, middle cup contains powder that has been struck by a spark and has not ignited, and the right cup contains powder that has bee struck by a spark and has ignited.

The electrode cup on the left shows powder that has not been struck by a spark. The middle cup shows powder that has been struck by a spark but did not ignite. A small crater approximately 2-3mm in diameter can be seen in the center. For all tests, typical crater diameters of displaced powder were between 1 and 3mm in diameter, and were always formed whether or not sufficient energy was supplied to the powder to cause ignition. The last cup on the right shows Mg powder that has been struck by a spark and

the spark energy was sufficient to ignite the powder. There is a white oxide layer covering almost the entire powder surface. It should be noted that the oxidation layer formed after the spark was over as the surface of the powder away from the crater was observed to burn for several seconds. The oxidation layer serves as qualitative evidence that ignition has occurred. The ignition could also be registered from the green filtered emission trace which is shown in Figure 4.2. It is interesting that the strong increase in the green signal emission is observed after a long (~ms) delay following a short, ~10μs pulse produced by the electric spark. It was observed that the green filtered emission traces of powder with and without binder were comparable. All further discussed ESD ignition experiments are for the powder/binder composition.

4.2 Ignition Delay

Ignition delay as seen in Figure 4.2, is the time difference between the spark and the moment at which the signal begins to increase. A consistent procedure for identification of this moment is necessary to consider various experimental trends. To aid in determining the point of ignition, a straight line was overlaid on the straight portion of the signal increase and was projected to the base of the signal. The point of intersection between the projected line and the base signal was the ignition moment, shown in Figure 4.2. Figure 4.3 shows the ignition delay as a function of capacitance at the minimum ignition energy required to ignite the powder. The voltage for each capacitance was incremented in 0.5kV steps in determining the minimum ignition energy, and 20 discharges were applied at 0.5kV lower than the minimum ignition threshold to establish the energy at which no ignition occurs.

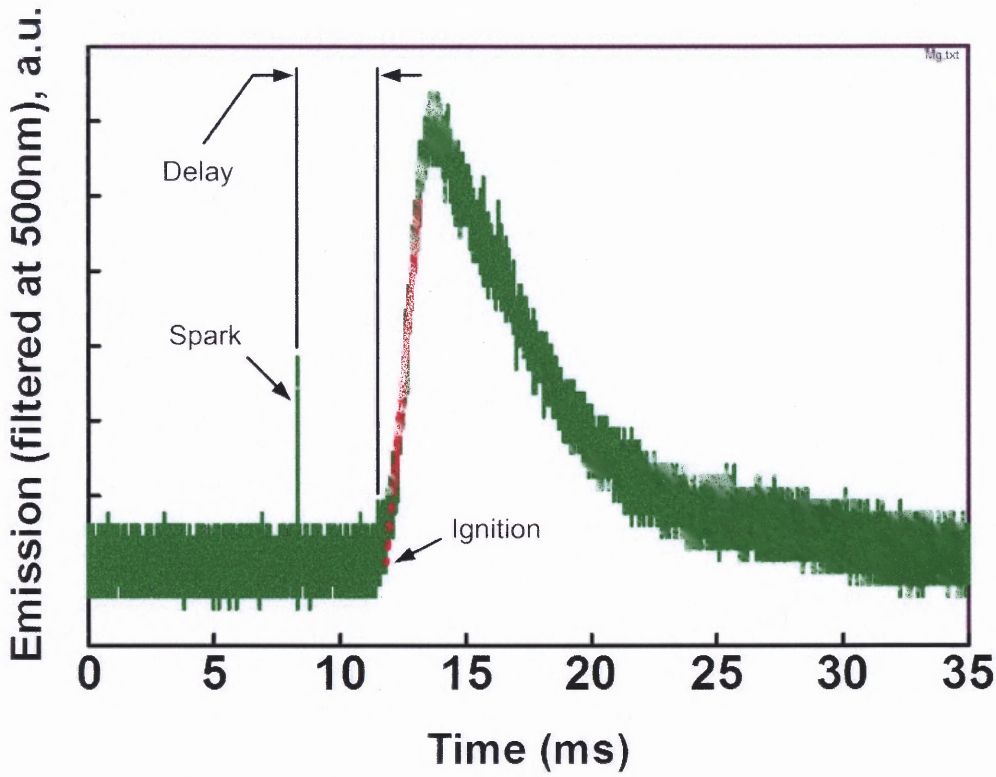

Figure 4.2 Example of green (500nm) filtered oxidation of Mg which shows the ignition of the Mg in the electrode cup.

The applied resistance, R_A is 0Ω and the powder surface to tip spacing is 0.2mm. The error bars show the standard deviation between the ignition delays measured in the repeated experiments. The ignition delay does not appear to be a function of capacitance at the minimum ignition energy. Ignition delays at particular capacitances as a function of voltage are shown in Figures 4.4-4.5. Figure 4.4 shows the ignition delay for a capacitance of 2000pF at 5kV, 7kV, and 9kV and Figure 4.5 shows the ignition delay for a capacitance of 10000pF at 3kV, 4kV, and 5kV.

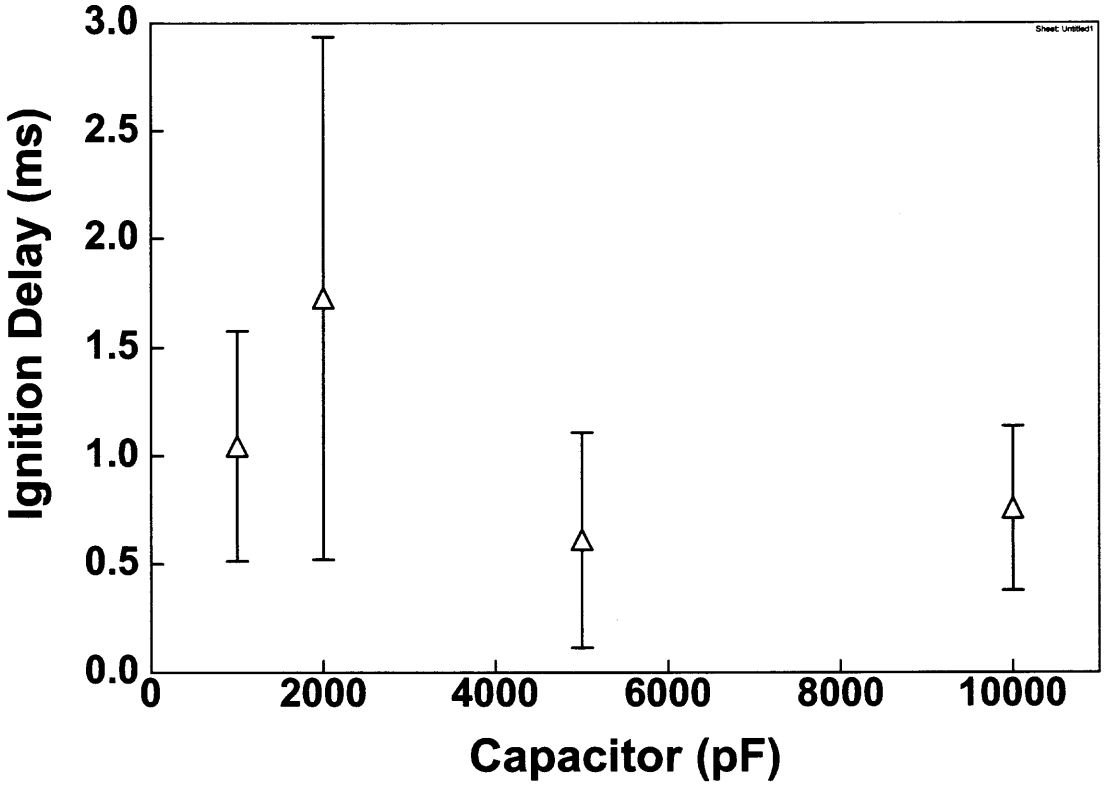

Figure 4.3 Ignition delay as a function of capacitance at the minimum ignition energy required to ignite the powder at 10000pF, 5000pF, 2000pF, and 1000pF (The corresponding voltages are 2.5kV, 3kV, 5kV, and 8kV, and the corresponding energies are 31mJ, 23mJ, 26mJ, and 34mJ).

For either capacitance, there is no obvious trend either and there are significant error bars. There is no obvious effect of capacitance and voltage on ignition delay. Instead, the range of delays at which ignition occurs which appears to be consistently around 0.5-1.5ms.

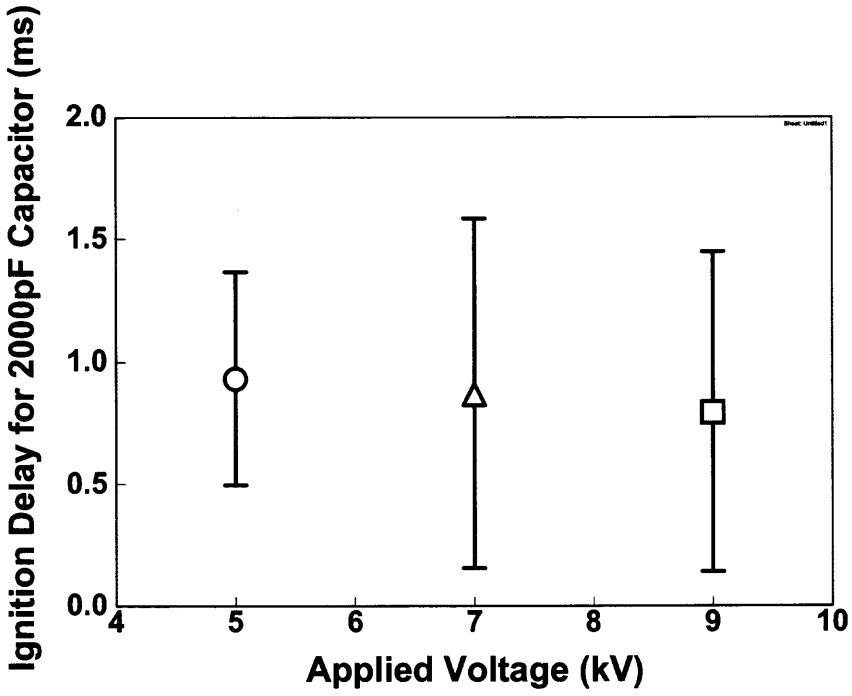

Figure 4.4 Ignition delay as a function of voltage (5kV, 7kV, and 9kV) at 2000pF.

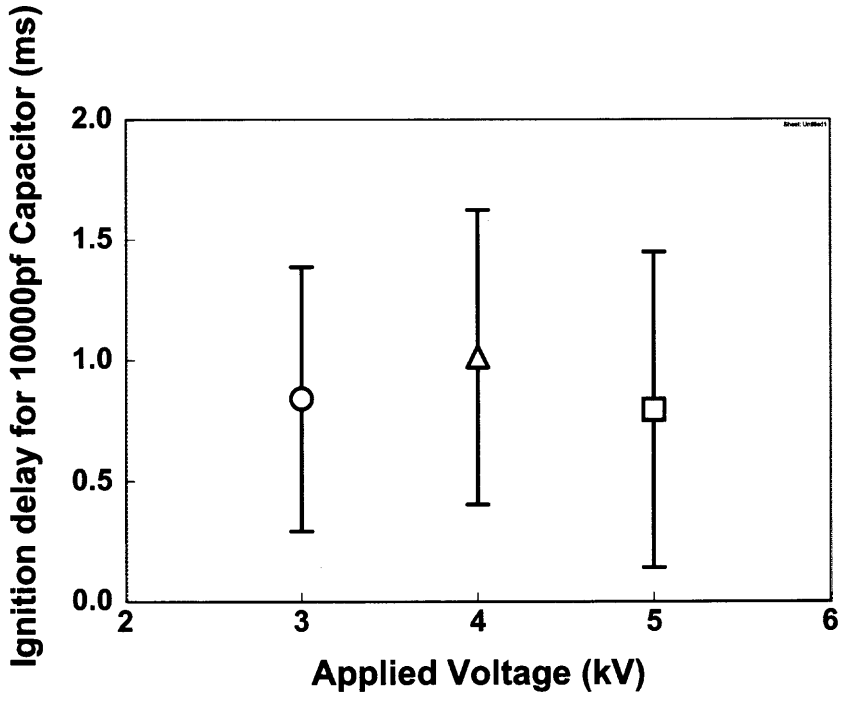

Figure 4.5 Ignition delay as a function of voltage (3kV, 4kV, and 5kV) at 10000pF.

4.3 Model Verification

As the numerical model takes several assumptions to the heat transfer that goes within the powder bed, it is important to verify heat transfer relationships with a known analytical solution. The only term that can be tested against a known solution is the conduction inside powder volume. To test conduction, all other heat transfer terms are disallowed. Also the effect of melting and boiling is disallowed, and there is no change in thermal conductivity. The energy input is a constant heat flux in a 1-D semi-infinite solid which is [21]:

$$T(x,t) = T_i + \frac{2q''}{k}\sqrt{\frac{\alpha t}{\pi}}\exp\left(-\frac{x^2}{4\alpha t}\right) - \left(\frac{q''x}{k}\right)\left(1 - erf\left(\frac{x}{2\sqrt{\alpha t}}\right)\right) \tag{4.1}$$

where x is the position in the body, t is time, T_i is the initial temperature of the solid, q" is the energy flux, α is the thermal diffusivity of the solid, and k is the thermal conductivity of the solid. The numerical model is run and the temperature distribution is allowed to equilibrate within the volume. A comparison of the dimensionless temperature of both the numerical and analytical solutions of the temperature distributions are shown in Figure 4.6. The temperature distributions are nearly identical and only slightly diverge deeper within the powder volume. Therefore a reasonable agreement between the temperature distributions of the numerical model with the analytical solutions guarantees that the error in determining conduction within the powder bed is negligible.

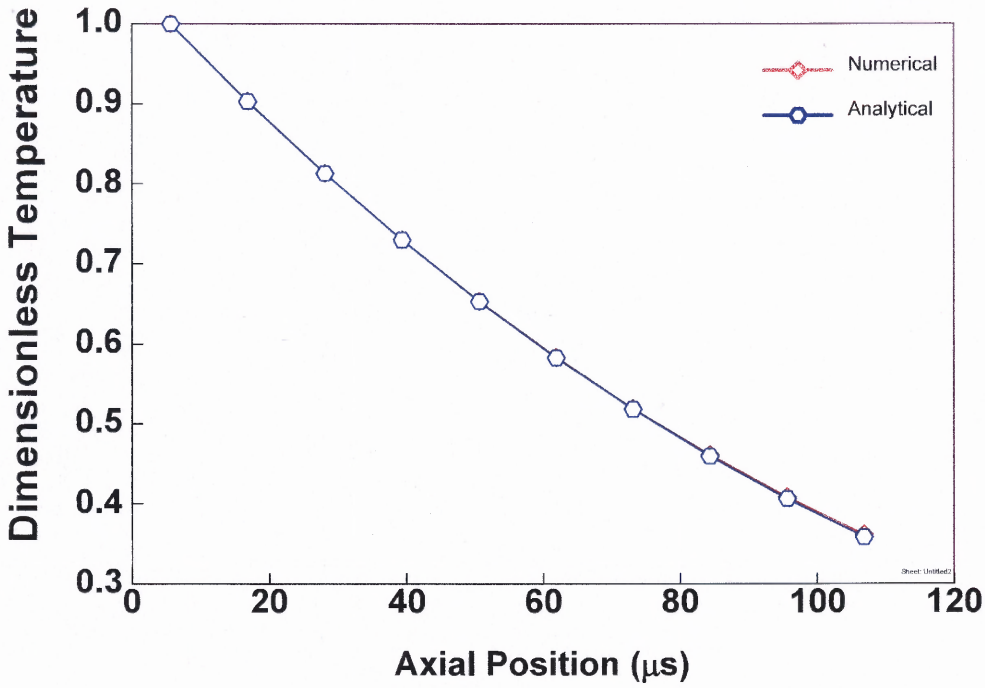

Figure 4.6 Comparison between the analytical and numerical solutions.

4.4 Preliminary Model Results

Simulations were run which modeled the actual current decay obtained in the current calibration measurements. The mechanism by which the energy is transferred to the powder bed from the spark is unknown. It could be transferred primarily to the top layer of the powder as a result of its direct interaction with the discharge plasma. Alternatively, the powder can be heated by the current passing through it an effect referred to as "Joule heating" below. The effect of non-Joule heating and Joule heating within the powder bed was tested. For the case of the powder surface being heated by the discharge directly, the energy was delivered to the powder surface as a heat flux assuming a Gaussian distribution described by Equation 3.15. The temporal exponential decay was described in Equation 3.16. The temperature distribution predicted for that case is shown in Figure

4.7. Each element of the numerical mesh is selected to represent a 10μm particle, the mean particle size of the Mg powder used in ignition tests. When an element boils off, its color changes white. Boiling of one or more of the mesh elements is expected to indicate an ignition event. Melting occurs at 923K and boiling occurs at 1380K [22]. Assumption of the ESD energy transfer to the powder from the powder surface only produces extremely sharp temperature gradients within the powder. Such gradients are developed because the thermal conductivity of the powder is relatively low while the rate of energy transfer from the discharge to the exposed elements (particles) is very high. As a result, a very small powder volume is heated and boiled very rapidly, and ignition occurs well within the spark duration which is not seen in Mg ignition experiments.

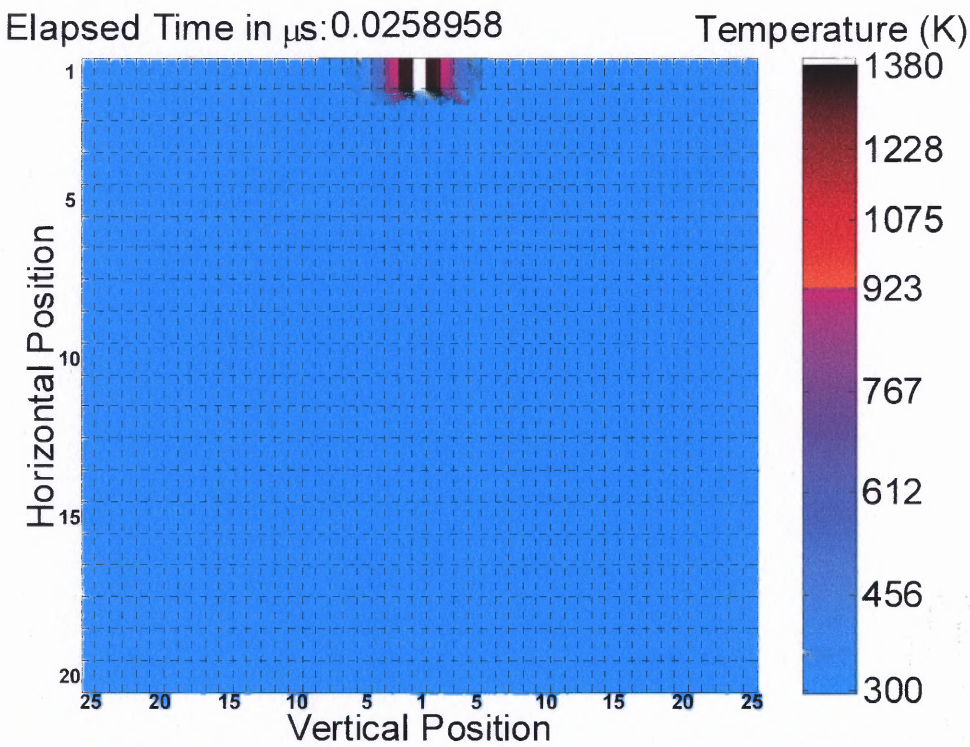

Figure 4.7 Temperature distribution within the powder bed for the case of non-Joule heating which leads to ignition during the spark duration.

For the case of Joule heating, the current distribution and decay along the particle surface was modeled according to Equations 3.15-3.16. The Joule heating at the powder contact resistances is described by Equations 3.12-3.14. The temperature distribution for the Joule heating case is shown in Figure 4.8. The distribution shown is spherical with protrusions around its periphery. The protrusions are predicted to form when a relatively wide molten pool is produced. Both thermal and electrical conductivities in the melt are much greater that in solid powder. Therefore, asymmetric current patterns are developed on opposite sides of the molten pool resulting in an increased heating rate in selected locations. This effect will be altered once a more realistic change of electrical and thermal conductivities as a function of temperature is used in the program.

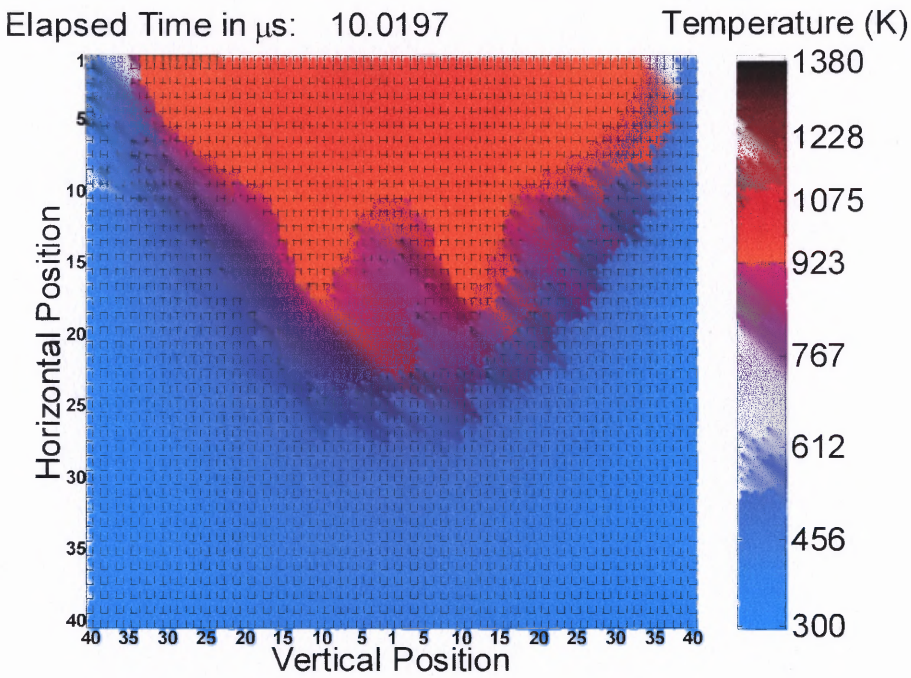

Figure 4.8 Temperature distribution within the powder bed for the case of Joule heating which does not lead to ignition during the spark duration.

When Joule heating within the powder volume is considered the heating of the powder bed occurs much slower and the temperature is distributed over a relatively large domain. The temperature distributions are significantly affected by the assumed effect of temperature on the electric conductivity of the powder.

It is interesting the molten pool predicted to form during the spark discharge remains after the spark is over, as shown in Figure 4.9. It appears that the heat of chemical reaction occurring near the Mg melting point is sufficient to maintain the pool stable despite heat losses to the unheated powder.

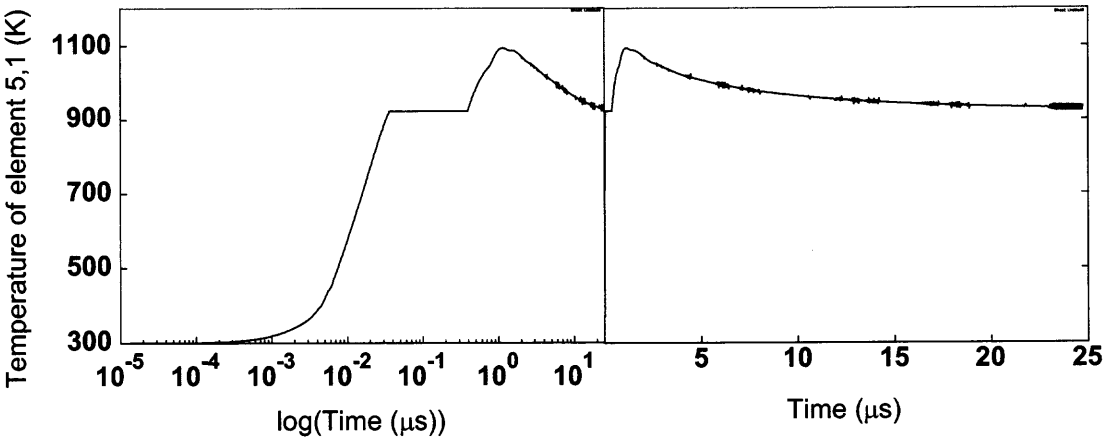

Figure 4.9 Temperature as a function of time for element 5,1 (on the left within the first 5μs there is a distinct period of melting followed by further heating to 1100K and followed by cooling; on the right the element is clearly seen cooling and stabilizes at the melting temperature at 25μs).

CHAPTER 5

CONCLUSIONS

The firing test system used in standardized ESD sensitivity tests was calibrated and prepared for detailed measurements. It was found that the spark duration is of the order of a few μs. The current in the spark produced by the discharge apparatus was observed to have a significant AC component. The spark polarity was not observed to affect the direct heating of a metallic substrate. A portion of powder was observed to be ejected by the spark discharge so that a crater forms under the pin electrode. The ejection occurs with or without associated powder ignition. Preliminary experiments on Mg ignition show a significant decay (0.5-1.5ms) between the spark pulse and the rise in the radiation signal due to the powder combustion. This delay was not affected by discharge voltage or capacitance.

A heat transfer model was developed to determine whether the thermal initiation is the main cause of powder ignition under the ESD stimulation. The model considers the conductive heat transfer in a powder bed, which is controlled by the thermal resistance of particle contacts. The model relies on an experimentally determined thermal diffusivity in the powder bed. The model considers Joule heating as a major mechanism of heat transfer from the discharge to the powder. It also includes convection and radiation heat transfer terms. The chemical reaction is introduced and described by an Arrhenius function. The limitations on the reaction rate due to the finite rate of oxygen diffusion to the reacting surface are also considered.

In the future, the model will take into account the changes of thermal conductivity and resistivity over a wider ranger of temperatures. The model will be validated for a

wide range of powders and testing conditions and used to study and understand the mechanisms of ESD ignition sensitivity of reactive materials. Parametric studies, both computational and experimental, will be conducted to establish the effect of the discharge power, duration, electrode material and shape and other parameters on the ESD sensitivity of selected reactive powders. The effect of gas environment will be addressed in particular. The findings from the study will then be incorporated into the ignition model to further the understanding of ESD powder ignition processes.

APPENDIX

CONTENTS OF THE ATTACHED COMPACT DISK

The descriptions below refer to the contents of the attached compact disk (CD). "Current calibration.xls" is the file that contains the current calibration data. The "Raw Curve_Fit" spreadsheet contains the raw values of current decay obtained from the shunting the experimental apparatus as described in Chapter 2, with the combinations of voltages, capacitances, and resistances used to obtain current decay as given in Table 2.3. The "RI Average-STD" spreadsheet contains the individual wire resistance R_I values as well as the average value of R_I and its standard deviation. In "10000pF", "5000pF", "2000pF", "1000pF", "500pF", "250pF", and "100pF" contains plots of the raw and fit curves of the current decay. On "5kV-10000pF-0ohm", "5kV-10000pF-500ohm", "10kV-10000pF-500ohm", "5kV-5000pF-0ohm", "5kV-5000pF-500ohm", "10kV-5000pF-500ohm", "10kV-2000pF-1500ohm", "10kV-2000pF-5000ohm", "15kV-2000pF-5000ohm", "15kV-1000pF-1500ohm", "15kV-1000pF-5000ohm", "20kV-1000pF-5000ohm", "20kV-500pF-1500ohm", "20kV-500pF-5000ohm", "25kV-500pF-5000ohm", "15kV-250pF-5000ohm", "20kV-250pF-5000ohm", "20kV-100pF-5000ohm", and "25kV-100pF-5000ohm" spreadsheets contains the measured energy for each voltage, capacitance, and resistance combination as well as comparison to the potential energy delivered.

"Optical calibration.xls" is the file that contains the optical signal calibration data. Contained on the "SS Target-Neg Pol", "SS Target-Pos Pol", "Al Target-Neg Pol", and "Al Target-Pos Pol" spreadsheets is the raw data for combinations of cup substrate, polarity, and capacitance of optical measurements made as mentioned in Chapter 2.

"Period of oscillations" shows the same plot as in Figure 2.7, and "Oscillation start to peak" and "Peak to decay" shows the same plots as in Figure 2.8. Contained in "Time periods" spreadsheet are all data values used in producing the plots. "Example of all traces" shows the same plots as in Figures 2.5, 2.6, and 2.8.

There are three main files for the Mg ignition delay results. "Mg ignition experiment capacitance.xls" contains the Mg ignition delay results for the case of varying capacitance while keeping voltage and resistance fixed. The green emission traces are contained in "10000pF", "5000pF", "2000pF", and "1000pF" spreadsheets. The ignition delays and other results obtained are contained in the "Results summary" spreadsheet. The plot of ignition delay as a function of capacitance is contained in "Delay" and was used to make Figure 4.4. "Mg ignition experiment 10000pF capacitance.xls" contains the Mg ignition delay results for the case of varying voltage above the minimum ignition energy for 10000pF capacitance. The green emission traces are contained in the "Data" spreadsheet. The "Results summary" spreadsheet contains the ignition delay and other results. "Delay" shows the same plot as Figure 4.6. "Mg ignition experiment 2000pF capacitance.xls" contains the Mg ignition delay results for the case of varying voltage above the minimum ignition energy for 2000pF capacitance. The green emission traces are contained in the "Data" spreadsheet. The "Results summary" spreadsheet contains the ignition delay and other results. "Delay" shows the same plot as Figure 4.5.

There are two main m files for the numerical model. "Discharge_Model_v2_2.m" file contains the main routine for describing heat transfer within a powder bed. Joule heating is contained in the "spark_v2.m" function. The main discharge model describes the main heat transfer terms as described in Chapter 3. To model a particular powder, the

material properties are changed as appropriate. Also to model the spark, the total resistance, total capacitance, and applied voltage is selected which describes the current and rate of decay. These parameters are sent to the "spark_v2.m" which computes voltages of each particle in the bed. From voltages and known resistance the heat dissipated across each contact is computed. The energy dissipated across each contact resistance is sent back to the main routine where it is added to the other heat transfer energy terms.

REFERENCES

1. Skinner, D., Olson, D., and Block-Bolton, A., 1997, "Electrostatic Discharge Ignition of Energetic Materials," Propellants, Explosives, Pyrotechnics, 23, pp. 34-42.

2. Mellor, A. M., and Stoops, D. R., 1990, "Optimization of Spark and ESD Propellant Sensitivity Tests," Propellants, Explosives, Pyrotechnics, 15, pp. 1-7.

3. Mellor, A. M., and Baker, P. J., 1994, "Propellant properties conducive to electrostatic discharge ignition," Journal of Energetic Materials, 12:1, pp. 1-62.

4. Raun, R. L., 2000, "Modeling of ESD-Induced Confined Ignition of Solid Rocket Propellants," Combustion and Flame, 120, pp. 107-124.

5. Makino, A., 2001, "Fundamental aspects of the heterogeneous flame in the self-propagating high-temperature synthesis (SHS) process," Progress in Energy and Combustion Science, 27, pp. 1-74.

6. Pearse, R.W.B. and Gaydon, A. G., 1976, *The Identification of Molecular Spectra* (4th ed.), Chapman and Hall, London, UK.

7. NIST Atomic Spectra Database v3, 2007, Atomic Spectra Peaks. Retrieved June 1, 2007 from http://physics.nist.gov/PhysRefData/ASD/index.html.

8. Arcor Electronics, Co., 2006, Nickel-Chromium Wire Resistance Data. Retrieved Aug. 1, 2007 from http://www.arcorelectronics.com/uninsulatedwire/Nickel_Chromium_Resistance_Wire.html.

9. Borghese, A., D'Alessio, A., Diana, M., and Venitozzi, C., 1988, "Development of hot nitrogen kernel, produced by a very fast spark discharge," Twenty-Second Symposium (International) on Combustion/The Combustion Institute, pp. 1651-1659.

10. Star Brite, Co. 2007. MSDS for liquid electric tape. Retrieved September 1, 2007 from http://www.starbrite.com/msdssheets/84104-msds-email-1-17-07.pdf.

11. NIST Chemistry WebBook 2007, Properties of acetone. Retrieved September 1, 2007 from http://webbook.nist.gov/cgi/cbook.cgi?ID=C67641&Units=SI&Mask=4#Thermo-Phase.

12. Cengel, Y.A., 2003, *Heat Transfer, a Practical Approach* (2nd ed.), McGraw-Hill, New York, NY.

13. Parker, W.J., Jenkins, R.J., Butler, C.P., and Abbott, G.L., 1961, "Flash method of determining thermal diffusivity, heat capacity, and thermal conductivity," Journal of Applied Physics, 32 (9), pp. 1679-1684.

14. Holman, J. P., 1981, *Heat Transfer* (5th ed.), McGraw-Hill, New York, NY.

15. Meaden, G. A., 1965, *Electrical Resistance of Metals*, Plenum-Press, New York, NY.

16. Ward, T.S, Trunov, M.A., Schoenitz, M., and Dreizin, E.L., 2006, "Experimental methodology and heat transfer model for identification of ignition kinetics of powered fuels," Heat and Mass Transfer, 49, pp. 4943-4954.

17. Bazyn, T., Krier, H., and Glumac, N., 2005, "Oxidizer and pressure effects on the combustion of 10-μm aluminum particles," Journal of Propulsion and Power, 21 (4), pp. 577-582.

18. Bazyn, T., Glumac, N., Krier, H., Ward, T.S., Schoenitz, M., and Dreizin, E.L., 2007, "Reflected Shock Ignition and Combustion of Aluminum and Nanocomposite Thermite Powders," Combustion Science and Technology, 179, pp. 457-476.

19. Li, S.C., & Williams, F.A., 1993, "Ignition and combustion of boron particles," *Combustion: Boron-based solid propellants solid fuels*, CRC, Boca Raton, FL.

20. Geankoplis, C.J., 2003, *Transport Processes and Separation Process Principles (4th ed.),* Prentice Hall, Upper Saddle River, NJ.

21. Holman, J.P., 2002, *Heat Transfer* (9th ed.), McGraw-Hill, Boston, MA.

22. NIST Chemistry WebBook, 2006, Phase change properties of Mg. Retrieved December 1, 2006 from http://webbook.nist.gov/cgi/cbook.cgi?ID=C7439954 &Units=SI&Mask=4#Thermo-Phase.